Journal of Solid State Chemistry 184 (2011) 1576–1579

Contents lists available at ScienceDirect

Journal of Solid State Chemistry

journal homepage: www.elsevier.com/locate/jssc

Rapid Communication

Crystal structure of $Bi_{1-x}Tb_xFeO_3$ from high-resolution neutron diffraction

Stefan Saxin, Christopher S. Knee*

Department of Chemistry, University of Gothenburg, SE-412 96 Göteborg, Sweden

ARTICLE INFO

Article history:
Received 5 January 2011
Received in revised form
13 April 2011
Accepted 17 April 2011
Available online 22 April 2011

Keywords:
$BiFeO_3$
$GdFeO_3$
Structural transition
Neutron diffraction
Multiferroic

ABSTRACT

Samples of $Bi_{1-x}Tb_xFeO_3$, with $x=0.05$, 0.10, 0.15, 0.20 and 0.25, have been synthesised by solid state reaction. The crystal structures of the perovskite phases, characterised via Rietveld analysis of high resolution powder neutron diffraction data, reveal a structural transition from the *R*3*c* symmetry of the parent phase $BiFeO_3$ to orthorhombic *Pnma* symmetry, which is complete for $x=0.20$. The $x=0.10$ and 0.15 samples are bi-phasic. The transition from a rhombohedral to orthorhombic unit cell is suggested to be driven by the dilution of the stereochemistry of the Bi^{3+} lone pair at the *A*-site. The G-type antiferromagnetic spin structure, the size of the ordered magnetic moment ($\sim 3.8\ \mu_B$) and the T_N (~ 375 °C) are relatively insensitive to increasing Tb concentrations at the *A*-site.

1. Introduction

The presence of antiferromagnetic and ferroelectric order at room temperature has motivated numerous investigations of the multiferroic perovskite $BiFeO_3$ (see [1–4] for example and references therein). As a bulk material the formation of single phase $BiFeO_3$ is complicated both by the metastable nature of the material [5], and the volatility of bismuth oxide at elevated temperatures. Isovalent substitution of Fe^{3+} or Bi^{3+} has been demonstrated to improve phase purity and give enhanced magnetic and ferroelectric properties [6,7]. Low levels of lanthanide substitution at the *A*-site in particular enhance the dielectric properties due to a reduction in leakage currents linked to the elimination of oxygen vacancies [8].

A number of different crystal structures have been proposed for chemically modified $BiFeO_3$ variants. For *A*-site, lanthanide, substituted samples, a general transition from the *R*3*c* symmetry of $BiFeO_3$ to the orthorhombic *Pnma* (*Pbnm* setting is often used) space group of the $GdFeO_3$ structure occurs. However, several intermediate symmetries between these two end members have been reported, dependent on the lanthanide ionic size and concentration of the substituent [9,10]. The complexity of these systems is illustrated by the recent reports of the presence of an antiferroelectric $PbZrO_3$-type phase with *Pbam* symmetry for a narrow range of Nd and Sm concentrations ($\sim$15–20%) [11]. Other authors have reported bi-phasic (*R*3*c* and *Imma* phases) behaviour [12], or single phases with polar orthorhombic symmetries such as $Pn2_1a$ [13] for similar compositions. A factor that undoubtedly adds to the confusion in relation to crystal structure determination is the use of laboratory based powder X-ray diffraction (PXRD), which is relatively insensitive to the oxygen sub-lattice. Other factors such as phase segregation, sample purity and crystallinity also make definitive structural determination problematic.

In this communication results on the $Bi_{1-x}Tb_xFeO_3$ system are presented. Previous studies of the effect of Tb substitution have focused on the deposition of thin films. Wang and Nan [14] reported enhanced remnant and saturation polarisation on films obtained by a spin coating technique. Recently, Chen et al. [15] discovered a high piezoelectric coefficient in $Bi_{1-x}Tb_xFeO_3$ films grown via a metal organic deposition method. To the best of the authors' knowledge the present work is the first relating to the synthesis and structural characterisation of bulk samples. The polycrystalline materials have been studied using X-ray and high resolution neutron diffraction complemented by differential scanning calorimetery.

2. Experimental

Samples of $BiFeO_3$ (BFO) and $Bi_{1-x}Tb_xFeO_3$ ($x=0.05$, 0.10, 0.15, 0.20, 0.25) were synthesised via solid state reaction of intimately mixed oxides, Bi_2O_3, Fe_2O_3, Mn_2O_3 and (pre-dried) Tb_4O_7. All chemicals were supplied from Sigma-Aldrich at $\geq$99.9% purity. The initial heating step was at 600 °C, and the temperature was then increased in 50 °C increments with 10 h reaction times followed by thorough re-grindings. The final sintering occurred at 850 °C.

---

* Corresponding author. Fax: +46 (0)31 772 1394.
E-mail address: knee@chem.gu.se (C.S. Knee).

0022-4596/\$ - see front matter © 2011 Elsevier Inc. All rights reserved.
doi:10.1016/j.jssc.2011.04.028

Long scan (PXRD) data were collected using a Bruker D8 Advance diffractometer with a primary monochromator ($CuK\alpha_1=1.54056$ Å, 15–105° 2θ, 0.0197° step size). Neutron powder diffraction data were collected at room temperature on the HRPD instrument at the ISIS neutron and muon facility, UK. Data from the high resolution backscattering detector bank were analysed via the Rietveld method [16] using the GSAS programme [17]. The low angle detector bank revealed intense magnetic peaks that were fitted using a G-type model to estimate the ordered component of the magnetic moment of the Fe^{3+} ion.

DSC data were obtained for BFO, $Bi_{0.9}Tb_{0.1}FeO_3$ and $Bi_{0.8}Tb_{0.2}FeO_3$, in the range 25–500 °C using a simultaneous TG/DSC Netszch STA409 PC instrument. Powder samples were placed in platinum crucibles and heated under a flow of N_2 at 10 °C/min.

3. Results and discussion

Fig. 1 shows the long scan PXRD data obtained for the samples in the range $0.05 \leq x \leq 0.20$. A clear change in the crystal structure is apparent, along with a two phase region observed for the $x=0.10$ and 0.15 samples. For $x=0.2$ and 0.25 the dominant perovskite phase displays a pattern characteristic of the $GdFeO_3$ (*Pnma*) structure. Minor impurity phases of $Bi_2Fe_4O_9$ for $x=0.05$ and $Tb_3Fe_5O_{12}$ for $x \geq 0.20$ are seen, the latter suggesting that the solubility limit of Tb is reached between $x=0.15$ and 0.20.

Rietveld analysis of the neutron diffraction data from the $x=0.05$ sample ($Bi_{0.95}Tb_{0.05}FeO_3$) revealed that it is satisfactorily described in the parent *R*3*c* symmetry of BFO modelled in a hexagonal setting. The introduction of 5% terbium at the *A*-site produced a slight contraction (~0.15%) in both the *a* and *c* cell parameters compared to our reference BFO sample. The neutron patterns obtained for $x=0.20$ and 0.25 were first modelled using the non-polar *Pnma* structure, and excellent agreement to the diffraction profile along with stable refinements was obtained. In order to test the possibility of a polar symmetry as reported for $Bi_{1-x}Gd_xFeO_3$ samples [13], further analyses of the data were performed using the non-centrosymmetric $Pn2_1a$ space group that is a sub-group of *Pnma*. After careful introduction of the variables, refinements with agreement factors slightly lower than those achieved using the *Pnma* structure were obtained, e.g., $\chi^2=3.10$ for 40 variables using $Pn2_1a$ in comparison to $\chi^2=3.62$ for 32 variables. In the final cycles of the analyses of the $x=0.05$, 0.2 and 0.25 samples the occupancies of the oxygen sites were permitted to vary and no sign of significant oxygen deficiency was detected. The agreement achieved to the $Bi_{0.8}Tb_{0.2}FeO_3$ neutron data using the *Pnma* structural model is shown in Fig. 2.

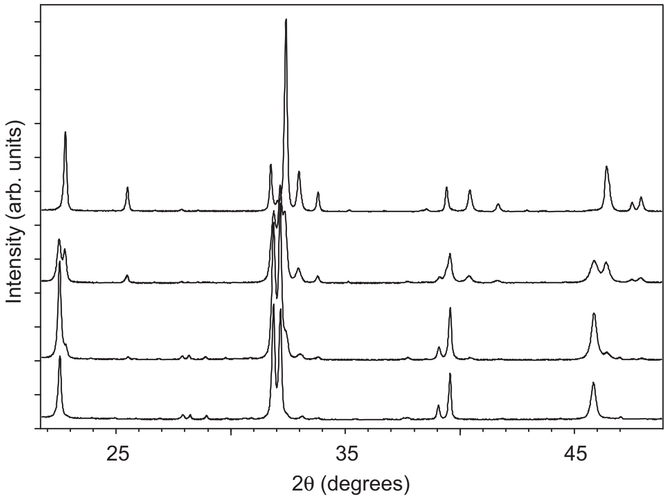

Fig. 1. Stack plot of a portion of the long scan PXRD data for the $Bi_{1-x}Tb_xFeO_3$ series for $x=0.05$ (bottom), $x=0.10$, $x=0.15$ and $x=0.20$ (top).

Due to its greater stability and the small difference in final quality of fit the *Pnma* model was used to model the orthorhombic component of the bi-phasic samples obtained for $x=0.10$ and $x=0.15$. Using this approach, stable refinements with ~10 and ~50 wt% of the orthorhombic phase were obtained for these samples. Attempts to refine the oxygen site occupancies of the bi-phasic samples proved to be unstable due to strong correlation caused by the phases sharing overlapping intensity. Furthermore, due to the similar neutron scattering lengths of Bi and Tb (8.53 and 7.38 fm, respectively), it was not possible to reliably refine the *A*-site occupancies for any of the phases investigated. These were therefore set at the initial target stoichiometry. Structural information obtained from the Rietveld analyses of the neutron data is summarised in Table 1 (*R*3*c* phases) and Table 2 (*Pnma* and $Pn2_1a$ analyses). Derived bond distances and Rietveld fits for all compositions are included in the supplementary data.

Comparison of the two orthorhombic structures used to model the crystal structures of $Bi_{0.80}Tb_{0.20}FeO_3$ and $Bi_{0.75}Tb_{0.25}FeO_3$

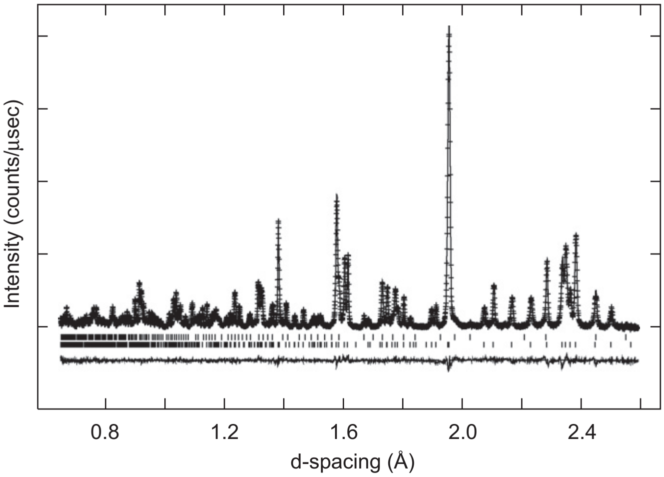

Fig. 2. Rietveld fit achieved to the backscattering detector bank of HRPD for $Bi_{0.8}Tb_{0.2}FeO_3$ using a *Pnma* structural model. Crosses are observed data points, upper line the calculated diffraction profile and lower line the difference between observed and calculated intensities. Tick marks indicate the position of reflections from $Bi_{0.8}Tb_{0.2}FeO_3$ (lower) and $Tb_3Fe_5O_{12}$ (upper).

Table 1
Refined structural parameters for *R*3*c* phases of $Bi_{1-x}Tb_xFeO_3$, $x=0.05$, 0.10 and 0.15, determined from Rietveld analysis of data collected at RT on HRPD.

Space group	$x=0.05$ *R*3*c*	$x=0.10$ *R*3*c*	$x=0.15$ *R*3*c*
Bi/Tb (0,0,*z*)	0.04680(11)	0.04524(13)	0.04466(23)
U_{iso} (Å^2)	0.72(4)	0.76(4)	1.08(7)
Fe (0,0,*z*)	0.26838(9)	0.26783(12)	0.26805(19)
U_{iso} (Å^2)	0.48(4)	0.43(4)	0.27(5)
O (***x***,*y*,0)	0.4438(2)	0.4421(3)	0.4448(5)
(*x*,***y***,0)	0.0170(3)	0.0167(3)	0.0188(5)
U_{iso} (Å^2)	0.88(3)	0.93(4)	1.24(4)
a (Å)	5.57263(4)	5.56616(5)	5.56034(11)
c (Å)	13.8409(2)	13.8170(3)	13.7937(6)
Vol. (Å^3)	372.233(6)	370.728(9)	369.33(2)
wt%	96.2(1) [a]	90.37(1) [b]	57.6(1) [b]
χ^2	6.10	3.75	3.19
R_{wp} (%)	6.17	6.06	5.58
R_p (%)	6.02	6.12	5.52
μ (μ_B)	3.75(2)	3.98(2)	4.0(3)

[a] Second phase $Bi_2Fe_4O_9$.

[b] Second phase is *Pnma* perovskite.

Table 2
Refined structural parameters for $Bi_{1-x}Tb_xFeO_3$, $x=0.20$ and 0.25, determined from Rietveld analysis of data collected at RT on HRPD.

Structural model		Atoms	x	y	z	Uiso (Å^2)	R factors (%)
$Bi_{0.8}Tb_{0.2}FeO_3$ *Pnma* [a]							
a (Å)	5.62644(5)	Bi/Tb	0.04914(13)	0.25	0.9933(3)	1.14(2)	$R_{wp}=4.68$
b (Å)	7.80144(8)	Fe	0.0	0.0	0.5	0.31(2)	$R_p=4.61$
c (Å)	5.43049(6)	O(1)	0.4733(2)	0.25	0.0922(3)	0.70(2)	$\chi^2=3.62$
Vol. (Å^3)	238.368(4)	O(2)	0.2002(2)	0.54441(13)	0.1971(2)	0.69(4)	32 variables
μ (μ_B)	3.79(2)						
$Bi_{0.8}Tb_{0.2}FeO_3$ *Pn*2$_1$*a* [b]							
a (Å)	5.62640(5)	Bi/Tb	0.04932(13)	0.2491(7)	0.9927(2)	1.00(2)	$R_{wp}=4.42$
b (Å)	7.80143(8)	Fe	−0.0002(6)	0.0	0.5003(6)	0.23(2)	$R_p=4.38$
c (Å)	5.43044(6)	O(1)	0.4740(2)	0.2459(8)	0.0921(3)	0.64(3)	$\chi^2=3.10$
Vol. (Å^3)	238.364(4)	O(2)	0.1914(5)	0.5315(6)	0.1887(5)	0.98(7)	40 variables
μ (μ_B)	3.82(2)	O(3)	0.2908(5)	0.4431(6)	0.7056(5)	0.243(6)	
$Bi_{0.75}Tb_{0.25}FeO_3$ *Pnma* [a]							
a (Å)	5.62642(5)	Bi/Tb	0.04991(12)	0.25	0.9929(2)	0.73(2)	$R_{wp}=4.39$
b (Å)	7.78938(6)	Fe	0.0	0.0	0.5	0.07(1)	$R_p=4.33$
c (Å)	5.42311(5)	O(1)	0.4725(2)	0.25	0.0935(2)	0.35(7)	$\chi^2=3.13$
Vol. (Å^3)	237.675(3)	O(2)	0.19989(15)	0.54531(11)	0.1966(2)	0.63(6)	32 variables
μ (μ_B)	3.73(2)						
$Bi_{0.75}Tb_{0.25}FeO_3$ *Pn*2$_1$*a* [b]							
a (Å)	5.62643(4)	Bi/Tb	0.05001(11)	0.2509(7)	0.9926(2)	0.67(2)	$R_{wp}=4.12$
b (Å)	7.78933(6)	Fe	−0.0014(6)	0.0	0.5002(6)	0.07(1)	$R_p=4.13$
c (Å)	5.42312(5)	O(1)	0.4732(2)	0.2460(8)	0.0932(2)	0.35(2)	$\chi^2=2.76$
Vol. (Å^3)	237.674(3)	O(2)	0.1932(5)	0.5346(6)	0.1888(5)	0.67(7)	40 variables
μ (μ_B)	3.77(2)	O(3)	0.2931(5)	0.4441(5)	0.7048(5)	0.16(7)	

[a] Secondary phase $Tb_3Fe_5O_{12}$ (1.5 wt%).
[b] Secondary phase $Tb_3Fe_5O_{12}$ (3.5 wt%).

reveals that any differences are small (Table 2). In particular the FeO_6 octahedra are free from significant distortions, and the oxygen sub-lattice in both structures can be described in terms of the $a^-b^+a^-$ octahedral tilt system of Glazer [18], in which two anti-phase tilts and an in-phase tilt are present. The FeO_6 tilt system of $Bi_{1-x}Tb_xFeO_3$ therefore evolves from $a^-a^-a^-$ (*R*3*c* symmetry), in which three equal anti-phase rotations of the FeO_6 units are present, to a situation where one anti-phase tilt is replaced by an in-phase tilt. The magnitude of the in-phase tilt for $Bi_{0.8}Tb_{0.2}FeO_3$, determined from analysis of the neutron data in *Pnma*, is 11.7(1)°. The magnitude of the anti-phase tilts increases from 12.6(1)° in $Bi_{0.95}Tb_{0.05}FeO_3$ to 14.1(1)° for the $x=0.2$ sample, and increases further to 14.4(1)° for $x=0.25$. The present results differ from the highly distorted FeO_6 environment obtained from recent Rietveld analysis of PXRD data for $Bi_{0.8}Gd_{0.2}FeO_3$ by Khomchenko et al. [13] using a *Pn*2$_1$*a* model. In general, significant distortions of the BO_6 octahedra within perovskites are unusual, and we believe the unrealistic oxygen coordinates reported in Ref. [13] are attributable to the use of PXRD data.

Khomchencko et al. also noted that the quality of fit to the $Bi_{0.8}Gd_{0.2}FeO_3$ PXRD diffraction data is basically identical for both non-polar *Pnma* and polar *Pn*2$_1$*a* structural models, and the selection of the *Pn*2$_1$*a* symmetry for the $x=0.2$ sample was supported primarily by local piezoresponse force microscopy [13]. Inspection of the refined atomic positions presented in Table 2 indicates that tiny shifts of the Fe and Bi ions, e.g., ~0.007 Å, are the only differences of relevance to potential ferroelectric behaviour in $Bi_{1-x}Tb_xFeO_3$, $x \geq 0.2$. Therefore, given that the introduction of several more refinable atomic coordinates, including a third independent oxygen site, produced only a marginal enhancement in the quality of fit, and the final structures are basically identical, we presently conclude that the *Pnma* model is the best representation of the average structure of $Bi_{0.80}Tb_{0.20}FeO_3$ and $Bi_{0.75}Tb_{0.25}FeO_3$. Closer examination of the compositional range between $x=0.15$ and 0.20 is clearly justified in order to determine whether the sequence of transition follows the $R3c \rightarrow Pn2_1a \rightarrow Pnma$ route proposed for $Bi_{1-x}Gd_xFeO_3$ ($0 \leq x \leq 0.3$) [13].

The polar *R*3*c* structure of $BiFeO_3$ is stabilised primarily due to the stereochemically active nature of the lone pairs of the Bi^{3+} ions that results in ordered displacements along the [111] direction of an ideal cubic perovskite. The structural transition from rhombohedral to orthorhombic symmetry reflects the increasing level of Tb that acts to both decrease the average ionic radius of the *A*-site cation and reduce the influence/coherence of the Bi^{3+} lone pairs. Density functional studies of BFO indicate that the role of Bi 6*s* and O $2p_x$,$2p_y$ hybridisation is critical in the formation of the lone pair lobes [19], and therefore it is the latter factor, rather than the decrease in average ionic size, that is likely to be most critical in the stabilisation of the new orthorhombic structure. In this context it is noteworthy that the high temperature paraelectric phase of $BiFeO_3$ was recently found to adopt the *Pbnm* (*Pnma*) structure [20] ($T_{Curie} \approx 820\,°C$). In this case greater thermal motion of the Bi ions may be expected to disrupt the Bi–O hybridisation, again reducing the activity of the lone pair. The present results may be compared with recent findings for the $Bi_{0.9}Sm_{0.1}Fe_{1-x}Mn_xO_3$ series [21]. Here, a transition to *Imma* ($a^-b^0a^-$) symmetry for the $x=0.3$ sample was observed and it was suggested that this structure emerges as a natural intermediate between the $a^-a^-a^-$ and $a^-b^+a^-$ tilt schemes.

To probe the magnetic behaviour of the $Bi_{1-x}Tb_xFeO_3$ materials DSC was used to detect the antiferromagnetic ordering temperature ($T_{Néel}$) of the $x=0.0$, 0.1 and 0.2 samples (Fig. 3). The T_N of 376 °C obtained for $BiFeO_3$ compares well with literature values [2,4]. Comparison with the other scans reveal that the T_N is relatively insensitive to the increasing levels of Tb at the

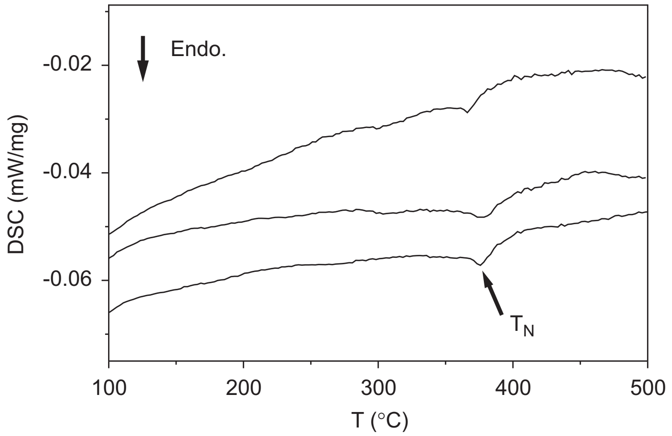

Fig. 3. Plot of the DSC data obtained for $Bi_{1-x}Tb_xFeO_3$, $x=0.0$ (bottom), $x=0.10$ (middle) and $x=0.20$ (top) samples on heating. The antiferromagnetic ordering temperature (T_N) is labelled for $BiFeO_3$.

A-site, although the structural transition results in a slight shift to lower temperature of approx. 10 °C for $Bi_{0.8}Tb_{0.2}FeO_3$. The ordered component of the magnetic moments determined from the neutron data (Tables 1 and 2) also remains fairly constant in the range 3.75–4.00 μ_B. The values are consistent with previous reports for BFO at RT [2,22] and reflect the presence of high spin Fe^{3+} ions ($S=5/2$). The agreement to the diffraction data obtained from the high *d*-spacing detectors is shown in the supplementary information.

Finally, it is valuable to compare our findings with the results reported previously for $Bi_{1-x}Tb_xFeO_3$ thin films [14,15]. The presence of diffraction peaks attributed to $TbFeO_3$ impurity lead Wang and Nan [14] to suggest the saturation limit of Tb is reached at $x=0.1$ for their samples. They also note that the main doublet in their PRXD data at $2\theta \approx 32^\circ$ merges to become a single peak for $x \geq 0.05$, and suggest both reduced crystallinity and/or a transition to tetragonal symmetry as possible reasons for this behaviour. In light of the current results it is worth considering whether the structural transition to orthorhombic symmetry was in fact observed in their lower resolution PXRD data, as it explains both the appearance of $TbFeO_3$ reflections and the peak coalescence. Similarly, we suggest that the transition noted at $x=0.11$ by Chen et al. [15] could be linked to the growth of an orthorhombic phase, probably *Pnma* or $Pn2_1a$. This composition reveals the highest saturation magnetisation and the largest remanent out-of-plane piezoelectric coefficient [15] (compatible with $Pn2_1a$), suggesting that strong magnetoelectric coupling can be expected at the cusp of the structural phase transition.

In summary the crystal structure of the $Bi_{1-x}Tb_xFeO_3$ ($0 \leq x \leq 0.25$) perovskites has been investigated. The transition to the orthorhombic $GdFeO_3$-type structure is attributed to a dilution of the effect of the Bi^{3+} lone pair as the Tb concentration increases. Further detailed characterisation of the dielectric and magnetic properties of the materials investigated here will be reported elsewhere.

Acknowledgments

The authors thank Aziz Daoud-Aladine, HRPD instrument, for the assistance with data collection. Experiments at the ISIS Pulsed Neutron and Muon Source were supported by a beamtime allocation from the Science and Technology Facilities Council.

Appendix A. Supporting information

Supplementary data associated with this article can be found in the online version at doi:10.1016/j.jssc.2011.04.028.

References

[1] J.R. Teague, R. Gerson, W.J. James, Solid State Commun. 8 (1970) 1073.
[2] P. Fischer, M. Polomska, I. Sosnowska, M. Symanski, J. Phys. C 13 (1980) 1931.
[3] F. Kubel, H. Schmid, Acta Crystallogr., Sect. B Struc. Sci. B46 (1990) 698.
[4] S.M. Selbach, M.-A. Einarsrud, T. Grande, Chem. Mater. 21 (2009) 169.
[5] G. Catalan, J.F. Scott, Adv. Mater. 21 (2009) 2463.
[6] J.R. Sahu, C.N.R. Rao, Solid State Sci. 9 (2007) 950.
[7] S.M. Selbach, T. Tybell, M.A. Einarsrud, T. Grande, Chem. Mater. 21 (2009) 5176.
[8] G.L. Yuan, K.Z. Baba-Kishi, J.-M. Lium, S.W. Or, Y.P. Wang, Z.G. Liu, J. Am. Ceram. Soc. 89 (2006) 3136.
[9] Z.V. Gabbasova, M.D. Kuzmin, A.K. Zvezdin, I.S. Dubenko, V.A. Murashov, D.N. Rakov, I.B. Krynetsky, Phys. Lett. A 158 (1991) 491.
[10] G.L. Yuan, S.W. Or, J.M. Liu, Z.G. Liu, Appl. Phys. Lett. 89 (2006) 052905.
[11] S. Karimi, I.M. Reaney, Y. Han, J. Pokorny, I. Sterianou, J. Mater. Sci. 44 (2009) 5102.
[12] I.O. Troyanchuk, M.V. Bushinsky, D.V. Karpinsky, O.S. Mantytskaya, V.V. Fedptova, O.I. Prochnenko, Phys. Status Solidi B 246 (2009) 1901.
[13] V.A. Khomchenko, V.V. Shvartsman, P. Borisov, W. Kleemann, D.A. Kiselev, I.K. Bdikin, J.M. Vieira, A.L. Kholkin, Acta Mater. 57 (2009) 5137.
[14] Y. Wang, C.W. Nan, J. Appl. Phys 103 (2008) 024103.
[15] X. Chen, G. Hu, W. Wu, C. Yang, X. Wang, S. Fan, J. Am. Ceram. Soc. 93 (2010) 948.
[16] H.M. Rietveld, J. Appl. Crystallogr. 2 (1969) 65.
[17] A.C. Larson, R.B. Von Dreele, Generalised Structure Analysis System Report LAUR86-748. Los Alamos National Laboratory, 2004.
[18] A.M. Glazer, Acta Crystallogr. B 28 (1972) 3384.
[19] P. Ravindran, R. Vidya, A. Kjekhus, H. Fjellvåg, O. Eriksson, Phys. Rev. B 74 (2006) 224412.
[20] D.C. Arnold, K.S. Knight, F.D. Morrison, P. Lightfoot, Phys. Rev. Lett. 102 (2009) 027602.
[21] S. Saxin, C.S. Knee, Dalton Trans. 40 (2011) 3462.
[22] I. Sosnowska, R. Przenioslo, P. Fisher, V.A. Murashov, J. Magn. Magn. Mater. 160 (1996) 384.